Electron nuclear double resonance study of pure and aquated rhodium complexes in silver chloride emulsions

1998 J. Phys.: Condens. Matter 10 11795

(http://iopscience.iop.org/0953-8984/10/50/018)

J. Phys.: Condens. Matter **10** (1998) 11795–11810. Printed in the UK PII: S0953-8984(98)96555-9

Electron nuclear double resonance study of pure and aquated rhodium complexes in silver chloride emulsions

Th D Pawlik, R S Eachus, W G McDugle and R C Baetzold

Imaging Research and Advanced Development, Eastman Kodak Company, 1669 Lake Avenue, Rochester, NY 14650, USA

Received 5 August 1998

Abstract. Detailed information has been obtained on the structure of pure and aquated Rh^{2+} complexes in AgCl using multifrequency EPR and powder ENDOR spectroscopy. Because of the anisotropy of the Rh^{2+} centre g matrix it was possible to selectively excite Rh^{2+} centres with a specific angle between the z axis of the g matrix and the magnetic field axis. As a result, almost single-crystalline-like ENDOR spectra were obtained and the angular dependence of the ENDOR spectra could be obtained by scanning the magnetic field over the range of the Rh^{2+} EPR spectra. Three different Rh^{2+} centres were detected that are distinguished by different thermal stabilities, different parameters of the g matrix and the hyperfine matrices of the central Rh nucleus and ligand H, Cl and Ag nuclei. A pure Rh^{2+} centre without H_2O ligands could only be generated in an emulsion where great care was taken to prevent the aquation of the $[RhCl_6]^{3-}$ dopant ion in the dopant solution and during the precipitation. This centre had the highest thermal stability. In an emulsion prepared conventionally two Rh^{2+} centres were found that are associated with one and two H_2O ligands bound to the Rh^{2+} ion in the plane perpendicular to the g matrix z axis. Using the results of the EPR and ENDOR analysis in combination with the results of a total energy calculation two models are proposed that contain the positions of the H_2O ligands and the charge compensating vacancies.

1. Introduction

Trivalent transition metal ions can be incorporated into melt-grown silver halide single crystals by addition to the melt and into photographic emulsions (i.e. silver halide microcrystals dispersed in gelatin) by coprecipitation from aqueous solution. The majority of such dopants occupy substitutional positions on the cation sublattice and serve as photoelectron traps. They can have a significant effect on the performance of silver halide materials [1–4]. $[RhCl_6]^{3-}$, because of its properties as a long-lived electron trap, is widely used as a dopant in some photographic products to increase contrast. $[RhCl_6]^{3-}$ is incorporated in the diamagnetic trivalent state and can be converted to the paramagnetic divalent state by photolysis or annealing in air above 300 °C. In AgCl single crystals, Rh^{2+} complexes have been studied by electron paramagnetic resonance (EPR) [5, 6] and electron nuclear double resonance (ENDOR) [7]. The EPR spectrum of Rh^{2+} is characterized by a largely axial anisotropic g matrix and partly resolved hyperfine structure from the interaction of the unpaired electron with two nearest neighbour Cl nuclei on the centre axis. The ENDOR studies in particular have led to a detailed microscopic model of the $[RhCl_6]^{4-}$ complex in the AgCl single crystal. In $[RhCl_6]^{3-}$-doped AgCl emulsions some resolution in the EPR spectrum is lost due to the arbitrary orientations of the AgCl microcrystals with respect to the magnetic field direction. Nevertheless, some characteristic features of the single crystal

0953-8984/98/5011795+16$19.50

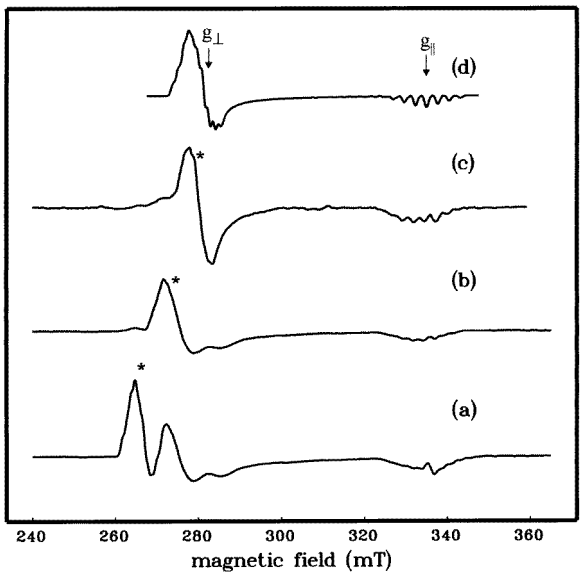

Figure 1. X band powder EPR spectra of $[RhCl_6]^{3-}$-doped AgCl emulsions measured at 9.42 GHz, $T = 10$ K. (a) Sample I after UV irradiation (365 nm) at 300 K. (b) Sample I after UV irradiation and annealing to 115 °C. (c) Sample II after annealing to 155 °C in the dark. (d) Simulated powder spectrum from data in [7].

EPR spectrum are preserved, namely the parallel and perpendicular g matrix components and the parallel component of the hyperfine interaction with the axial chlorine nuclei [8, 9].

$[RhCl_6]^{3-}$ complexes in aqueous solution have the propensity to exchange halide ligands with water molecules [10]. The incorporation of aquated Rh complexes was found to influence the sensitivity of the silver halide emulsion [11]. A recent EPR study assigned a complicated EPR spectrum from a UV-irradiated AgCl:$[RhCl_6]^{3-}$ emulsion to a superposition of signals from Rh^{2+} centres with different degrees of aquation [8]. ENDOR measurements [12] on these samples showed that the hyperfine interaction constants of one of these centres were very similar to the data obtained from the single crystal study. Unfortunately, the authors did not specify which of the Rh^{2+} centres was studied. In addition, no evidence was given for the presence of H_2O ligands. Schweizer and Spaeth [9] investigated the feasibility of powder ENDOR studies using NaCl:Rh^{2+} and AgCl:Rh^{2+} as model systems. In their ENDOR study on AgCl:Rh^{2+}, only weak lines originating from Ag nuclei along the g matrix z axis could be resolved for the magnetic field set to a value corresponding to $g_\perp$. The authors found that the Ag hyperfine interaction was significantly larger than that reported for the single crystal Rh^{2+} centre. Because of the lack of more experimental data, especially ENDOR lines from other ligands, no model for the Rh^{2+} centre complex in AgCl could be derived. Another group [13] studied Rh^{2+} centres in solution grown NaCl single crystals using ENDOR and found lines due to small hyperfine interactions with hydrogen nuclei. From the hyperfine interaction values it was concluded that the nuclei were at a distance of 18 Å (i.e. six times the Na–Cl distance) from the defect centre.

2. Experiment

The samples used in this investigation were produced as dispersions in aqueous gelatin by a double jet precipitation technique. The dopant was added as Na_3RhCl_6 to the NaCl

solution at a concentration of approximately 250 ppm. In one set of samples (hitherto named sample II) extreme care was taken to prevent the aquation of the $[RhCl_6]^{3-}$ complex. This was accomplished by using a highly concentrated and acidic Na_3RhCl_6/NaCl solution and by keeping this solution in the dark at ice temperatures. Another emulsion was made without control of the $[RhCl_6]^{3-}$ aquation. This emulsion will be referred to as sample I. For the EPR and ENDOR measurements the amount of gelatin peptizer was minimized by aqueous dilution and centrifugation cycles performed at 40 °C. This procedure leaves a residual layer of gelatin peptizer bound to the surface of the AgCl microcrystals. The samples were irradiated at room temperature with band gap light (365 nm) or annealed in the dark to about 155 °C.

The EPR and ENDOR measurements were performed on a highly modified Bruker ER-200D X band EPR/ENDOR spectrometer at 9.4 GHz. Optimum parameters for the ENDOR experiments were a sample temperature of 8–10 K and microwave power of 8 mW. The RF field was frequency modulated with modulation depths of 350 kHz or 100 kHz and a modulation frequency of 2 kHz. Q band EPR measurements were performed on a Varian E12 spectrometer operating at 35.3 GHz. The Q band measurements were carried out at 82 K.

3. Results

3.1. EPR measurements

Figure 1 shows powder EPR spectra of degelled AgCl:$[RhCl_6]^{3-}$ emulsions in three different preparation stages. Trace (a) corresponds to sample I after band gap irradiation at room temperature. Trace (b) shows the EPR spectrum of the same sample after an additional annealing stage at 115 °C for 5 min. Trace (c) shows the EPR spectrum of sample II after annealing to 155 °C in the dark. The same EPR spectrum can be obtained with somewhat lower intensity by band gap irradiation at RT. Finally, in trace (d) a simulated powder EPR spectrum for the $[RhCl_6]^{4-}$ complex in Rh-doped AgCl single crystals is shown. It was calculated using the data from [7]. The features corresponding to the parallel and perpendicular components of the g matrix are indicated in the figure. All experimental spectra are consistent with a d_{z^2} ground state since $g_\perp > g_\parallel \approx g_e$ [6] (g_e is the g value of the free electron). For a pure $d_{x^2-y^2}$ ground state one would expect $g_\parallel > g_\perp > g_e$. It is evident that, of the three experimental spectra, trace (c) matches most closely the simulated spectrum of the single crystal centre. Room temperature UV irradiation of sample I produces at least two rhodium centres that differ in the value of the perpendicular g matrix component (trace (a)). The centre with the higher $g_\perp$ can be destroyed by annealing to 115 °C as shown in trace (b). Further annealing to 145 °C destroys the second centre. In sample I no Rh^{2+} centres can be generated by annealing in the dark.

For further reference we will label the Rh^{2+} defect that is generated in sample I by UV irradiation at room temperature (RT), and that decays at 115 °C, as the 'low temperature centre'. The defect with the higher thermal stability will be labelled the 'medium temperature centre'. Finally, the Rh^{2+} defect generated in sample II by annealing to 155 °C in the dark will be labelled the 'high temperature centre'. The annealing step at 115 °C does not lead to an increase in the medium temperature centre concentration. The low temperature centres can be recreated by re-irradiation at RT. Therefore, it is unlikely that the low temperature centre is converted into the medium temperature centre through a structural relaxation. We think that the centres are separate defects with different thermal stability of the electron trapped state.

In the X band EPR measurements it was not possible to resolve a difference in the parallel g matrix component of the three Rh^{2+} centres. Furthermore, any orthorhombic component of the g matrix (known to exist for the single crystal Rh^{2+} centre) was hidden in the EPR linewidth. These ambiguities were removed by Q band EPR measurements. Figure 2 shows Q band EPR spectra at the same sample preparation stages as in figure 1. The orthorhombic components of the g matrices of the high temperature and medium temperature centres are clearly seen as splittings of the $g_\perp$ features in traces (b) and (c). Within experimental error the parallel components of the g matrices are the same for both centres. The g matrix of the low temperature centre is almost axially symmetric with the parallel component of the g matrix, somewhat smaller than in the case of the other two centres. This makes it possible to resolve the hyperfine structure at $g_\parallel$ of the low temperature centre which, in the X band, is superimposed on the parallel feature of the medium temperature centre. We will discuss this in conjunction with the ENDOR results in a later paragraph. At higher measurement temperatures (90–300 K) we observe an increase in the orthorhombic component (i.e. $|g_x - g_y|$) of the g matrix of the medium temperature centre. The EPR spectrum of the low temperature centre remains unchanged up to RT. From the Q band measurements we obtain g matrix parameters summarized in table 1. The g matrix components of the single crystal Rh^{2+} centre and the 'high temperature' centre are very similar. Therefore, it is likely that the defect structures of the Rh^{2+} centre in the Rh^{3+}-doped single crystal and the aquation controlled Rh^{3+}-doped emulsion (sample II) are similar. In order to verify this and to study the structural differences of the three different Rh^{2+} centres in the emulsions we undertook powder ENDOR measurements.

Table 1. g matrix parameters of three different Rh^{2+} centres in AgCl at 82 K. Estimated uncertainties are ± 0.005.

Centre	g_x	g_y	g_z
Single crystal [7]	2.426	2.395	2.011
Low temperature	2.548	2.538	1.986
Medium temperature	2.492	2.442	2.018
High temperature	2.436	2.406	2.018

3.2. ENDOR measurements

3.2.1. Introduction to powder ENDOR spectroscopy of defects with anisotropic EPR spectra. ENDOR spectroscopy of paramagnetic defects in powders can be divided into two distinct subclasses:

(i) If the defect has an isotropic EPR spectrum the EPR transition will involve defects with arbitrary orientations with respect to the magnetic field axis. Since there is no angular selection, the ENDOR spectrum will be powder-like (i.e. consist of narrow lines if the hyperfine interaction is isotropic or of powder patterns if the hyperfine interaction is anisotropic).

(ii) If the defect has an anisotropic EPR spectrum and the x, y and z features of the g matrix are well separated in the EPR spectrum, one can use the magnetic field position to selectively excite centres with certain orientations with respect to the magnetic field axis.

Clearly, the latter situation applies to the Rh^{2+} defects addressed in this study.

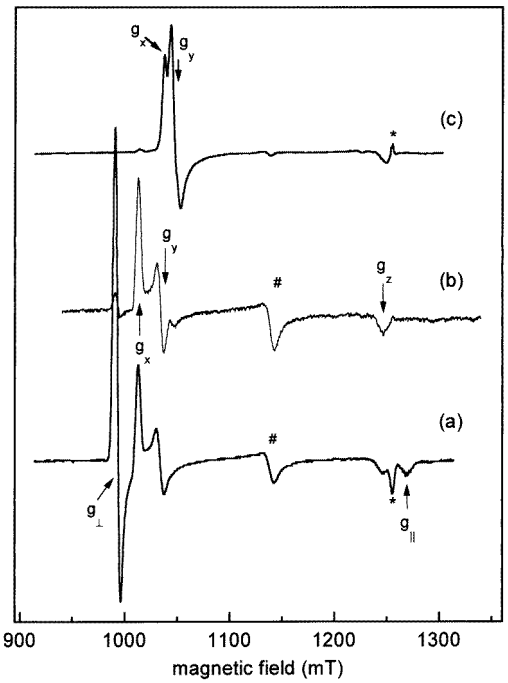

Figure 2. Q band powder EPR spectra of $[RhCl_6]^{3-}$-doped AgCl emulsions measured at 35.35 GHz, $T = 82$ K. (a) Sample I after UV irradiation (365 nm) at 300 K. (b) Sample I after UV irradiation and annealing to 115 °C. (c) Sample II after annealing to 155 °C in the dark. The features labelled with an asterisk are due to radical centres in the residual gelatin. The features labelled with a hatch are probably averaged EPR spectra due to rapid motion of one of the Rh^{2+} complexes at the temperature of the measurement (see, e.g., 7).

The angular selection can lead to results somewhat similar to the ENDOR angular dependence of a defect in a single crystal. Orientation selection in ENDOR spectroscopy of powders was first reported by Rist and Hyde [14]. A general theory has been developed by Hoffmann *et al* [15] and Hurst *et al* [16] including finite EPR component linewidths. In this paragraph we will limit ourselves to a qualitative discussion of a special case in which the g and hyperfine matrices are considered axially symmetric with the z axis being the axis of symmetry of the g matrix. Nucleus 1 is on the z axis, while nucleus 2 is in the xy plane. Setting the magnetic field to a value within the EPR spectrum will select centres with an angle α between the g matrix z axis and the magnetic field axis. A number of ENDOR spectra taken at different magnetic field values will have this angle as a variable parameter.

The positions of the ENDOR lines from nuclei 1 and 2 are defined by the angular dependent hyperfine interaction, which, for axial symmetry, is:

$$A(\alpha') = a + b(3\cos^2\alpha' - 1) \tag{1}$$

where a represents the isotropic hyperfine interaction and b the axially symmetric part of the anisotropic hyperfine interaction. Because the z axes of the g and hyperfine matrices are the same for nucleus 1, the angles α and α' are also the same. As a result, the selection of a single α via the magnetic field will result in a single α' for the ENDOR spectrum and the ENDOR spectrum will consist of single lines rather than powder patterns. When using frequency modulation the lines will have a symmetric derivative shape.

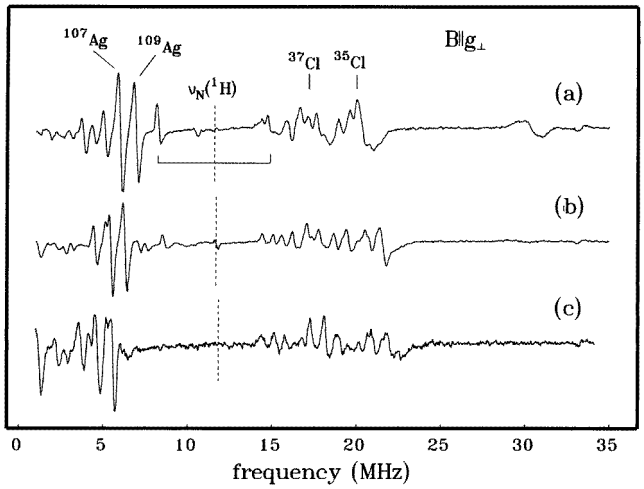

Figure 3. X band powder ENDOR spectra of $[RhCl_6]^{3-}$-doped AgCl emulsions measured at 9.42 GHz, $T = 10$ K in the feature of the EPR spectrum corresponding to $g_\perp$. (a) Sample I after UV irradiation (365 nm) at 300 K measured at $B = 266$ mT. (b) Sample I after UV irradiation and annealing to 115 °C measured at $B = 274$ mT. (c) Sample II after annealing to 155 °C in the dark measured at $B = 280.6$ mT. The asterisks in figure 1 denote the magnetic field positions for the three ENDOR spectra. The ^{1}H Larmor frequency is indicated by a dashed line.

For nucleus 2 the situation is different. If the magnetic field is set to a position corresponding to $g_\perp$ (i.e. $\alpha = 90°$), the magnetic field vector can have any orientation within the xy plane. Therefore α' can span all values between 0 and 90°. As a result, the ENDOR spectrum is powder-like and spans all values between $A_\parallel = A(0°)$ and $A_\perp = A(90°)$. If the magnetic field is shifted towards $g_\parallel$, the span of angles is reduced to $(90° - \alpha) < \alpha' < 90°$ thereby narrowing the powder pattern until at $\alpha = 0°$ the powder pattern is reduced to a single line at $A_\perp$.

Obviously the case of nucleus 1 will result in the simplest ENDOR spectrum. If the parameters of the g matrix are known, α and α' can be determined from the magnetic field value. Since each individual EPR line has a nonzero linewidth (e.g., broadened by hyperfine interaction), the value α should be considered as a narrow distribution of angles around α with a certain distribution width. This distribution of angles will result in a broadening of ENDOR lines. Therefore, it can be expected that, despite the angular selectivity of this method, the resolution of a single crystal ENDOR spectrum will not be reached.

3.2.2. ENDOR results. Figure 3 shows X band powder ENDOR spectra of $[RhCl_6]^{3-}$-doped AgCl emulsions measured at 9.42 GHz, $T = 10$ K in the features of the EPR-spectra corresponding to the $g_\perp$ positions. The asterisks in figure 1 denote the magnetic field positions for the three ENDOR spectra. Due to the selection of the magnetic field and the preparation of the samples the three spectra should correspond to the low temperature centre (trace (a)), medium temperature centre (trace (b)), and high temperature centre (trace (c)).

All three ENDOR spectra consist of lines around 5 MHz and between 15 and 23 MHz. The former can be identified as being due to Ag interactions. The two isotopes of Ag (^{107}Ag and ^{109}Ag) have a similar nuclear g factor and are almost equally abundant. Therefore, Ag interactions can be easily identified by the appearance of pairs of lines with equal intensity and a ratio of frequencies of 1.15 corresponding to the ratio of nuclear g factors. In the

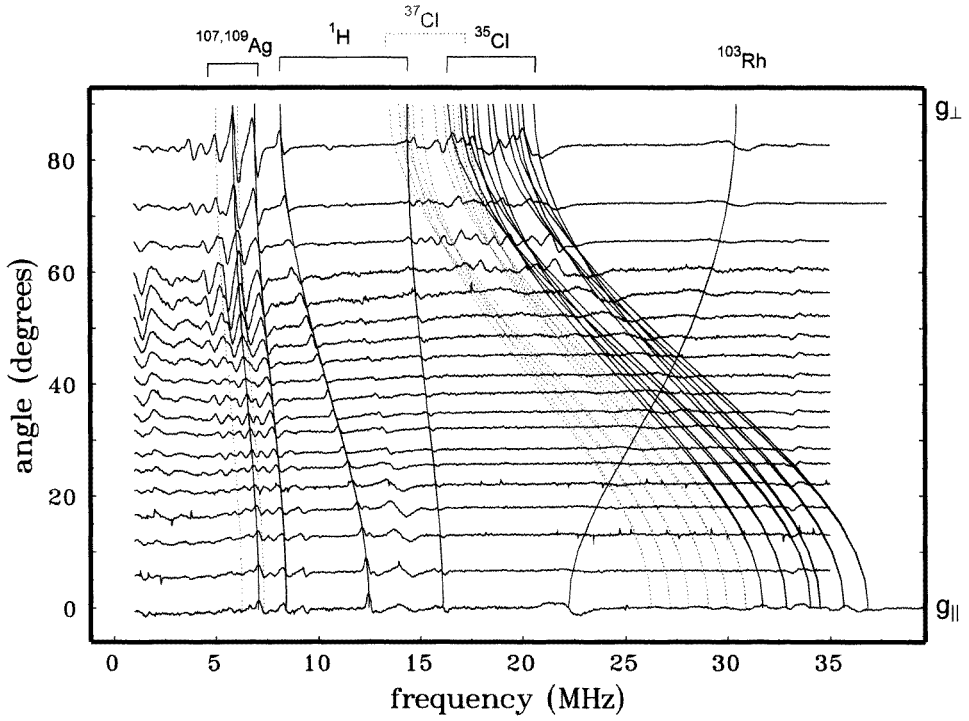

Figure 4. ENDOR angular dependence of the low temperature Rh^{2+} centre. For the definition of the angle, see text.

single crystal ENDOR study [7] lines from Ag nuclei in this frequency range were attributed to the second shell axial (i.e. on the g matrix z axis) Ag nuclei. The lines between 15 and 23 MHz could be due to Cl interactions. They lie in the same frequency range as the ENDOR lines attributed to axial chlorine nuclei in [7]. In both cases it should be expected that the position of the nuclei on the z axis should result in single-crystal-like ENDOR spectra.

In addition to the common features of the ENDOR spectra, there are certain lines that do not appear in all spectra: A line at 30 MHz is unique to the ENDOR spectrum of the low temperature centre. A pair of lines at 8 MHz and 14 MHz appears in the ENDOR spectra of the low and medium temperature centres. The lines are spaced symmetrically about the Larmor frequency of ^{1}H at 11.5 MHz (note that this fact is much more visible in the field dependences of figures 4 and 5, which will be discussed later). Figure 4 shows the angular dependence of the low temperature centre ENDOR spectra as a stack-plot of spectra measured at different field values. The angle α was calculated using the g matrix values for the low temperature centre and the spectra are positioned vertically so that the y axis position of the baseline corresponds to the angle α. The solid and dashed curves are calculated ENDOR line positions for the axial chlorine and silver nuclei and for the ENDOR lines attributed to hydrogen and rhodium.

3.2.3. ^{35,37}Cl ENDOR lines. The complicated spectrum of the chlorine ENDOR lines results from splittings due to quadrupole interaction Q, which is allowed for all nuclei with

a spin of $I > 1/2$. It results in a splitting of a single ENDOR line into $2I$ lines. In the case of ^{35,37}Cl I is $3/2$ resulting in a total of 12 lines for the two m_S states and two isotopes. In addition, it was observed in the single crystal study [7] that the chlorine hyperfine and quadrupole interaction shows a considerable non-axiality. Such non-axiality will lead to a further doubling of ENDOR lines in the 83° spectrum, since the g_x and g_y components of the g matrix are not separated in the X band so that ENDOR spectra due to both A_x, A_y and Q_x, Q_y are observed.

Figure 4 shows that the chlorine ENDOR spectrum becomes broad and unresolved for angles away from the $g_\parallel$ and $g_\perp$ field positions. For the determination of the parameters of the chlorine quadrupole and hyperfine interaction we therefore took only the two ENDOR spectra at the extreme positions of $\alpha = 0°$ and 83° into account and attempted an ENDOR lineshape analysis. The resulting ENDOR line positions for the intermediate angles are shown as the solid and dashed curves for the ^{35}Cl and ^{37}Cl isotope, respectively.

3.2.4. ^{107,109}Ag ENDOR lines. The ENDOR spectra of the axial Ag nuclei are much simpler. There are two isotopes of almost equal abundance both with a nuclear spin of $I = 1/2$ and therefore, no quadrupole interaction. The two solid curves in figure 4 are calculated ENDOR frequencies for the $m_S = -1/2$ sublevel of the Rh^{2+} system. The dashed curves represent the ENDOR frequencies of the corresponding $m_S = +1/2$ sublevel. They are found to be lower in intensity by a factor of two to three. The Ag ENDOR lines can be followed over the whole range of angles. The spectra are always single-crystal-like thus supporting the assignment to Ag nuclei on the g matrix z axis.

3.2.5. ^{1}H ENDOR lines. ENDOR lines attributed to ^{1}H can be seen in the frequency range between 8 and 17 MHz. They are equally spaced about the ^{1}H Larmor frequency, which is field dependent and ranges from 11.28 MHz at 0° to 14.27 MHz at 83°. At angles close to 90° the ^{1}H ENDOR spectrum shows features of a powder pattern (i.e. the ENDOR lines in the frequency modulated spectra do not have a symmetric derivative shape), which supports the assignment of the lines to ^{1}H nuclei in the equatorial plane. The ^{1}H ENDOR lines are much narrower than the lines due to Ag and Cl nuclei. Thus, they can be separated from the Cl and Ag lines by reducing the frequency modulation amplitude. This is shown in figure 5 as a stack-plot of ENDOR spectra measured at different magnetic field positions (indicated on the y axis) in the region of $g_\perp$ of the low and medium temperature centres. 100 kHz frequency modulation amplitude was used. The spectra are plotted with a variable x-axis offset, so that the field-dependent ^{1}H Larmor frequency corresponds to 0 MHz. This way, the ENDOR lines corresponding to the two m_S levels of the same nucleus are equally spaced about 0 MHz. For reasons of clarity the ENDOR lines that are discussed in the following paragraph are plotted as thick black lines whereas the rest of the ENDOR spectra are plotted as thin black lines. The spectra measured at 266 mT and 274 mT correspond to the traces (a) and (b) in figure 3 which were measured with 350 kHz modulation amplitude. The field region between 262 and 270 mT corresponds to $g_\perp$ of the low temperature centre. The region between 270 and 280 mT corresponds to g_x and g_y of the medium temperature centre, which are separated by about 5 mT in the X band. In the former field range, the lines labelled by asterisks correspond to the ^{1}H lines that could be followed in the angular dependence of figure 4. In addition, there are narrow lines at ± 4.9 MHz (marked by hatch signs) that were obscured by the axial Cl and Ag ENDOR lines when the higher modulation amplitude was used. These lines could correspond to the third parameter of the hyperfine matrix. In the region of g_x and g_y of the medium temperature centre narrow lines appear

at similar positions. The non-axiality of the g matrix of the medium temperature centre is reflected in the appearance of the lines at ± 4.9 MHz and ± 3.2 MHz at different field positions corresponding to g_x and g_y, respectively. The analysis of the ENDOR angular dependence (figure 4) shows that the hyperfine matrix value for the ^{1}H interaction that corresponds to $B_0 \| g_z$ is 3.6 MHz. With the above information we can assign the hyperfine matrix values of 9.6 MHz to $B_0 \| g_x$ and 6.4 MHz to $B_0 \| g_y$ of the low temperature centre. The assignment of the hyperfine matrix values of the medium temperature centre is made accordingly.

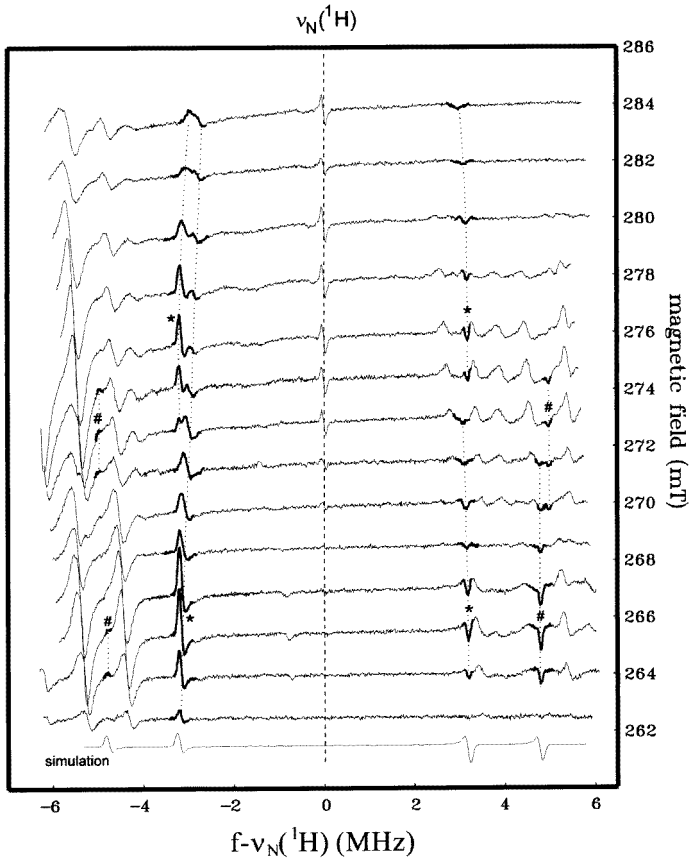

Figure 5. ENDOR spectra of the low and medium temperature Rh^{2+} centres measured at different magnetic field values (indicated on the right y axis) with a frequency modulation amplitude of 100 kHz. The ENDOR lines discussed in the text are grouped by dotted lines. The labels $*$ and # are explained in the text. The lowest trace is a calculated ENDOR spectrum for the equatorial ^{1}H nuclei with the magnetic field in the xy plane.

In the paragraph discussing the Ag ENDOR lines it was mentioned that the ENDOR lines corresponding to the different m_S states ($m_S = +1/2$, $m_S = -1/2$) differ in intensity by a factor of two to three, with the lines corresponding to $m_S = -1/2$ being the stronger ones. The same holds true for the ^{1}H ENDOR lines (compare the intensity of the lines marked with asterisks at ± 3.2 MHz). The lines marked with hatch signs have the opposite intensity relation with the line at $+4.9$ MHz being higher in intensity than the line at -4.9 MHz. This suggests that the hyperfine matrix values for the features at ± 3.2 MHz

and ±4.9 MHz have the opposite sign. For a positive hyperfine interaction the stronger ENDOR lines ($m_S = -1/2$) should be at the positive side of the Larmor frequency (which is true for the lines at ±4.9 MHz). Accordingly, the lines at ±3.2 MHz correspond to a negative hyperfine interaction.

We can define a local coordinate system (x', y', z') for the hyperfine interaction of the equatorial ^{1}H nuclei in which $A_{z'}$ corresponds to the hyperfine matrix value for B_0 parallel to the line between the central ^{103}Rh nucleus and the ligand ^{1}H nucleus. This direction can be either x or y, depending on whether the ^{1}H nucleus is put at (100) or (010), respectively. The values for the hyperfine matrix of the low temperature centre for the two cases are shown in table 2.

These values are related to the isotropic hyperfine constant a and the anisotropic hyperfine interaction constants b (axial) and b' (non-axial) by [17]:

$$A_{x'} = a - b + b' \qquad A_{y'} = a - b - b' \qquad A_{z'} = a + 2b. \tag{2}$$

In both cases the isotropic hyperfine interaction constant is very small ($a = -0.13$ MHz). For the case $z' \| x$ the hyperfine interaction matrix is largely axial with $b = 4.9$ MHz and $b' = 1.4$ MHz, whereas for $z' \| y$ it is largely non-axial with $b = -3.3$ MHz and $b' = -6.6$ MHz.

Table 2. Hyperfine matrix parameters for the equatorial ^{1}H nuclei of the low temperature centre. Estimated uncertainties are ±0.05 MHz for $A_{y'}$ and $A_{z'}$ and ±0.1 MHz for $A_{x'}$.

	$A_{x'}$ (MHz)	$A_{y'}$ (MHz)	$A_{z'}$ (MHz)
$z' \| x$	−3.6	−6.4	9.6
$z' \| y$	−3.6	9.6	−6.4

The low isotropic ^{1}H interaction can be explained by the small overlap of the Rh^{2+} wavefunction with the 1s orbital of the H atom leading to a small transfer of unpaired spin density. The anisotropic hyperfine interaction should be dominated by the point dipole–dipole interaction, which is directly related to the electron nuclear separation by:

$$b = 95.625 \text{ MHz} \frac{g_N}{(r/r_B)^3} \tag{3}$$

where g_N is the nuclear g factor (5.585 69 for ^{1}H), r is the electron–nuclear separation and r_B is the Bohr radius [17]. The non-axial component of the hyperfine interaction reflects the non-spherical distribution of the electron wavefunction and the non-coincidence of the g tensor and hyperfine tensor z axes. This parameter is usually smaller than the axial component, therefore we see the assignment $z' \| x$ as more probable. The electron nuclear separation calculated using (3) for this case is $r = 4.78 r_B$ which is close to the Ag–Cl equilibrium distance at 0 K of $5.205 r_B$.

3.2.6. ^{103}Rh ENDOR lines. The ENDOR line in figure 4 that changes its position from 22 MHz at 0° to 31 MHz at 83° has a symmetric derivative shape pointing to an on-axis nucleus. The assignment of this line to a specific nucleus is made difficult by the fact that no line corresponding to the other m_S state is found in the frequency region from 1 to 60 MHz. Due to the anisotropic nature of the EPR spectrum one cannot use the field shift method to determine the nuclear g factor and thereby determine the isotope involved (for an explanation and examples of the field shift method, see e.g., [17]). However, one can exclude that this line is due to Ag or Cl, because both elements have two magnetic

isotopes with abundance ratios of roughly 1:1 for ^{107}Ag : ^{109}Ag and 1:3 for ^{35}Cl : ^{37}Cl, so that at least two lines would be expected for each m_S state (as in the case of the axial Ag ENDOR lines). The two remaining possibilities are an assignment to ^{1}H or to ^{103}Rh. In the former case the ENDOR line corresponding to the other m_S state would be expected at frequencies around 8 MHz or 50–53 MHz, depending on which m_S state it is assigned to. No corresponding ENDOR lines were seen in the spectrum. In the latter case, due to the small nuclear g factor of ^{103}Rh ($g_N = -0.1768$), the two lines would be separated by only 0.7 MHz, which is within the ENDOR linewidth. In order to distinguish between the two possibilities we prepared Rh-doped powder samples using D_2O and H_2O. The corresponding ENDOR spectra of the low temperature centre are shown in figure 6 for the H_2O sample (trace (a)) and for the D_2O sample (trace (b)). The magnetic field value corresponds to $g_\perp$. The comparison of traces a and b shows that the ^{1}H ENDOR lines at 8 and 16 MHz indeed disappear in the D_2O sample, whereas the line at 30 MHz is clearly present in both the D_2O and H_2O spectra. This shows that the latter line must be due to ^{103}Rh. In addition, the spectra show fine structure in the ^{103}Rh line. The three-line pattern can be explained by a superposition of lines due to the two m_S states (separated by 0.7 MHz) and a small non-axiality of 1 MHz in the hyperfine matrix. Note that the isotropic and anisotropic ^{103}Rh hyperfine interaction constants of the low and high temperature centre differ by almost one order of magnitude (table 5).

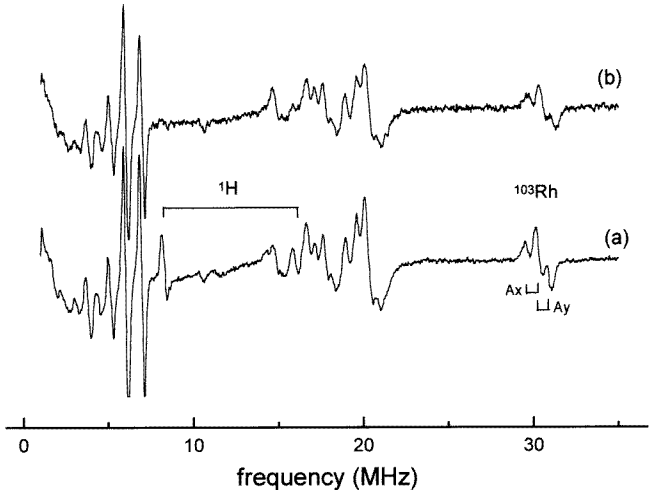

Figure 6. ENDOR spectra of the low temperature centre in samples prepared with H_2O (trace (a)) and D_2O (trace (b)). The ENDOR spectra were measured at $B = 266$ mT in the feature of the low temperature centre EPR spectrum corresponding to $g_\perp$.

For magnetic field positions close to $g_\perp$ there are lines in the ENDOR spectrum of the medium temperature centre that could be attributed to the central ^{103}Rh nucleus of this centre (figure 7). The resulting hyperfine matrix parameters are $A_x = 19.1$ MHz and $A_y = 22.4$ MHz. The value for A_z could not be determined because the lines could not be followed over the whole angular dependence. The values for A_x and A_y lie between those of the high temperature centre and those of the low temperature centre, thus reflecting the general trend observed for the axial Cl and Ag nuclei (see tables 3–6 and the discussion below). Furthermore, the large difference between A_x and A_y reflects the large non-axiality of the g matrix of the medium temperature centre.

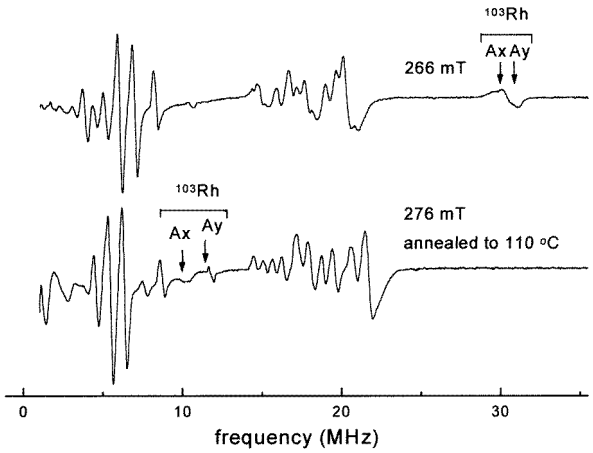

Figure 7. ENDOR spectra of the low temperature (upper trace) and medium temperature centre (lower trace) measured at magnetic field values corresponding to $g_\perp$. The ENDOR lines assigned to the ^{103}Rh hyperfine interaction are marked in the figure.

The analysis of the ENDOR angular dependence including all of the assignments made in the preceding paragraphs leads to the parameters for the hyperfine and quadrupole interaction constants summarized in tables 3–6.

Table 3. Axial ^{35}Cl hyperfine and quadrupole interaction constants. Estimated uncertainties are ± 0.2 MHz for the hyperfine matrix and ± 0.02 MHz for the quadrupole matrix parameters. q and q' are related to the components of the quadrupole matrix by $Q_x = -q + q'$, $Q_y = -q - q'$ and $Q_z = 2q$.

	A_x (MHz)	A_y (MHz)	A_z (MHz)	q (MHz)	q' (MHz)
Low temperature	37.8	36.2	68.5	0.20	< 0.01
Medium temperature	40.4	39.0	72.2	0.31	0.03
High temperature	41.6	39.7	77.5	0.41	0.06
Single crystal [7]	44.8	39.6	77.6	0.40	0.14

Table 4. Axial ^{109}Ag hyperfine interaction constants. Estimated uncertainties are ± 0.1 MHz.

	A_x (MHz)	A_y (MHz)	A_z (MHz)
Low temperature	12.8	12.8	15.5
Medium temperature	11.5	11.5	14.2
High temperature	9.7	9.7	12.7
Single crystal [7]	9.7	9.7	12.7

4. Discussion

The g matrix parameters and hyperfine and quadrupole interaction constants of the high temperature centre are very similar to those of the single crystal Rh^{2+} centre. In addition,

Table 5. Axial ^{103}Rh hyperfine interaction constants. Estimated uncertainties are ±0.3 MHz for the low- and medium temperature centre and 0.1 MHz for the high temperature centre.

	A_x (MHz)	A_y (MHz)	A_z (MHz)
Low temperature	60.5	61.5	44.2
Medium temperature	19.1	22.4	?
High temperature	6.9	5.3	9.3
Single crystal [7]	6.54	5.46	9.00

Table 6. Equatorial ^{1}H hyperfine interaction constants. Estimated uncertainties are ±0.05 MHz for $A_{y'}$ and $A_{z'}$ and ±0.1 MHz for $A_{x'}$.

	$A_{x'}$ (MHz)	$A_{y'}$ (MHz)	$A_{z'}$ (MHz)
Low temperature	−3.6	−6.4	9.6
Medium temperature	−3.2	−6.4	9.8
High temperature			
Single crystal			

there are no signals due to ^{1}H ligands. Therefore, it is reasonable to assume that both centres have the same microscopic structure, i.e. $[RhCl_6]^{3-}$ with a silver ion vacancy at (200).

Even without considering the ^{1}H ENDOR lines the observance of ENDOR lines from axial Cl and Ag nuclei can rule out centre models where the two axial Cl^- ions are replaced by H_2O. Furthermore, a charge compensation by two Ag^+ ion vacancies along the z axis is not possible. A replacement of one axial Cl^- ion by H_2O would render the two axial Ag nuclei inequivalent, which is not seen in the ENDOR spectra. One Ag^+ vacancy along the z axis would similarly remove the equivalence of the axial Cl ligands. The ENDOR results on the axial Cl and Ag ligands can only be explained if there are either two axial Ag and Cl ligands or one axial Ag and Cl ligand. The EPR spectrum can provide valuable information to distinguish between these two cases. For the low temperature centre the hyperfine structure of the EPR spectrum should be dominated by splittings due to the axial Cl nuclei and the central Rh nucleus. All other hyperfine interactions are so small that they are not resolved in the EPR spectrum. To test this experimentally we can study the feature in the Q band EPR spectrum corresponding to $g_\parallel$, which is separated from that of the medium temperature centre. Figure 8 shows in the lowest trace the experimental EPR spectrum in the field region corresponding to $g_\parallel$. The traces above are calculated powder EPR spectra using the hyperfine interaction constants determined in the ENDOR analysis for different numbers of Cl and Rh nuclei. The comparison shows that, indeed, the calculation with one Rh and two equivalent Cl nuclei matches closest the experimental spectrum. The $g_\parallel$ features of the medium and high temperature centre show resolved hyperfine structure in the X band EPR spectra. The seven line structure indicates that in both cases the splitting is due to two equivalent Cl nuclei.

The ENDOR lines corresponding to the ^{1}H interaction have a powder-like shape suggesting an H_2O ligand in the plane perpendicular to the g matrix z axis. Both the low and medium temperature centre have this ligand. It is possible that the low temperature centre has two equivalent H_2O ligands in the xy plane whereas the medium temperature centre has only one. Unfortunately, this could not be determined directly from the ENDOR

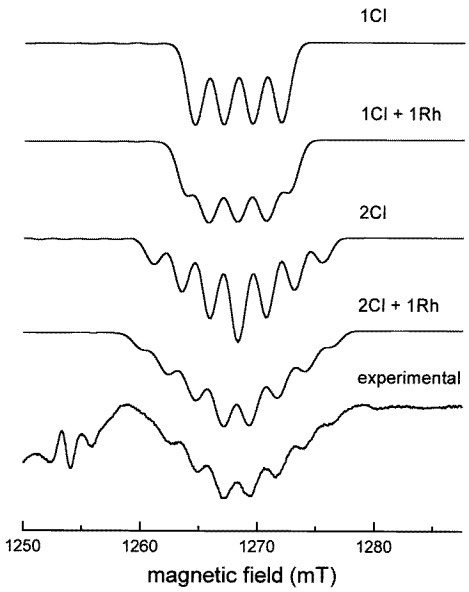

Figure 8. Experimental EPR spectrum (middle trace) and simulations of the parallel feature of the low temperature centre. Upper trace: simulation for one axial Cl^- ligand and the axial H_2O ligand with two equivalent ^1H nuclei. Lower trace: simulation for two axial Cl^- ligands.

analysis. In order to obtain a microscopic model for the low and medium temperature Rh^{2+} centres we have calculated the total energy for a number of different configurations of Rh^{2+} defects with one or two H_2O ligands in the first coordination shell and a corresponding arrangement of charge compensating Ag^+ vacancies. For full charge compensation the Rh^{2+} centre with one H_2O ligand (monoaqua), which we tentatively assign to the medium temperature centre, requires 2 Ag^+ vacancies while the centre with two H_2O ligands requires an additional third Ag^+ vacancy and is tentatively assigned to the low temperature centre. The number of possible models was greatly reduced by the experimental information from the EPR and ENDOR analysis. The experimental constraints were:

(i) The H_2O ligands must be in the xy plane.
(ii) No Ag^+ or Cl^- vacancies along the z axis.
(iii) The models should reflect the large non-axiality of the medium temperature centre and the near axiality of the low temperature centre.
(iv) The electron spin should be in a d_{z^2} orbital in order to account for the g matrix parameters ($g_\perp > g_\parallel \approx g_e$).

A number of structural models with different vacancy configurations were calculated using classical atomistic simulation procedures described in detail elsewhere [18]. They were based upon the use of short-range interatomic potentials and a polarizable ion description using a shell model. The interaction of water ligands with nearest-neighbour crystal ions was treated by a potential derived from quantum mechanical calculations. The water ligands were constrained to relax axially in the presence of vacancies. In table 7 the total vacancy binding energies are tabulated for several dopant–H_2O–vacancy configurations that are in accordance with the experimental constraints mentioned above. The total vacancy binding energy refers to the energy required to remove all vacancies from positions next

to the dopant to a remote part of the crystal. The two structural models with the highest vacancy binding energies are depicted in figure 9. In addition to the classical binding energy calculation we did Hartree–Fock calculations of each configuration in table 7. The complex was embedded within a point-ion lattice and its geometry was determined by optimization. In all cases, the unpaired electron predominantly occupied a d_{z^2} orbital on Rh and the axial Rh–Cl bond distances exceeded their equatorial counterparts. All centre models exhibit C_2 or lower symmetry allowing a non-axial g matrix. In the case of the low temperature centre, however, the arrangement of H_2O ligands and vacancies renders the Rh d_{xz} and d_{yz} orbitals degenerate which may account for the observed nearly axial symmetry of the g matrix.

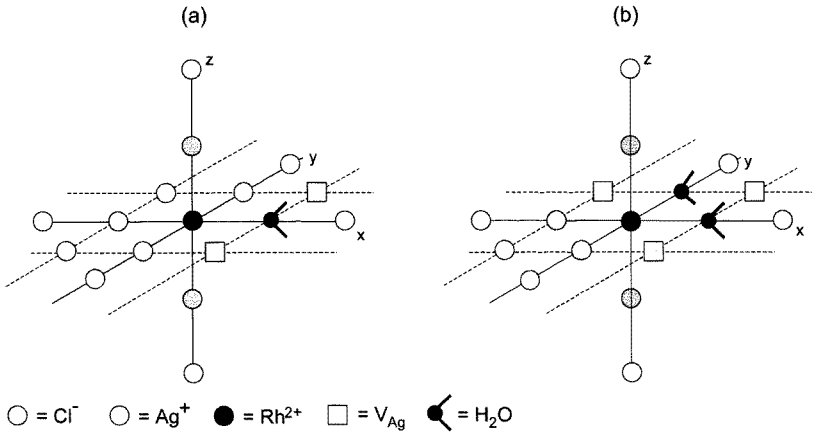

Figure 9. The structural models for the medium (a) and low temperature (b) Rh^{2+} centres in AgCl.

Table 7. Total vacancy binding energies calculated for various configurations of $[RhCl_5(H_2O)]^{n-}$ and $[RhCl_4(H_2O)_2]^{n-}$ centres. The Rh^{2+} ion is situated at (000).

	H_2O position(s)	Vacancy position(s)	Total vacancy binding energy (eV)
$[RhCl_5(H_2O)]^{3-}$	(100)	$(110)(1\bar{1}0)$	3.03
		$(101)(10\bar{1})$	2.49
		(110)(002)	2.86
$[RhCl_4(H_2O)_2]^{2-}$	(100)(010)	$(110)(\bar{1}10)(1\bar{1}0)$	3.66
		(110)(200)(020)	3.25
		$(110)(011)(10\bar{1})$	3.24
		$(\bar{1}\bar{1}0)(200)(020)$	3.20

The assignment of the low temperature centre to a diaqua complex is supported by the observation that the ratio of the low and medium temperature centre EPR signals after irradiation at RT depends on the time the dopant solution is allowed to aquate. With longer aquation times it changes in favour of the low temperature centre.

An interesting feature of the ENDOR spectra of the low and medium temperature centre is that the ENDOR line at the hydrogen Larmor frequency only appears in the case of the medium temperature centre (see figure 5). This ENDOR line is due to nuclei that are at large distances from the paramagnetic centre so that the hyperfine interaction consists only

of a very small point dipole–dipole interaction. The ENDOR linewidth can be used as an estimate of the lower limit of the separation (see, e.g., [19]). The appearance of the Larmor line only in the case of the medium temperature centre suggests that this centre is either situated nearer to the surface of the microcrystals and thus nearer to the ^{1}H nuclei in the residual gelatin, or that the medium temperature centre has the propensity to aggregate into clusters. In the latter case the ENDOR line at the Larmor frequency is due to H_2O ligands of other nearby Rh^{2+} centres.

If we compare the position of the $^{107/109}Ag$ ENDOR lines measured by Schweizer and Spaeth [9] with the corresponding line positions in the ENDOR spectra of the three Rh^{2+} centres in this study we conclude that the centre studied in [9] corresponds to the medium temperature centre we assign to the monoaqua (i.e. $[RhCl_5(H_2O)]^{3-}$) complex.

5. Conclusion

The present study has shown that powder ENDOR spectroscopy on defects with anisotropic EPR spectra can yield considerable structural information. In particular, the angular selection of defect centres via the selection of the magnetic field leads to almost single-crystalline-like ENDOR spectra with a high resolution and the possibility to generate an ENDOR angular dependence by scanning the magnetic field over the range of the Rh^{2+} EPR spectra. Q band EPR spectroscopy has proven valuable in assessing the axiality of the different Rh^{2+} centres. The results of the annealing experiments show that the aquated Rh^{2+} centres have a lower thermal stability than the pure $[RhCl_6]^{4-}$ centre.

References

[1] Eachus R S and Olm M T 1983 *Radiat. Eff.* **73** 69
[2] Corrigan D A, Eachus R S, Graves R E and Olm M T 1979 *J. Chem. Phys.* **70** 5676
[3] Eachus R S, Graves R E and Olm M T 1978 *J. Chem. Phys.* **69** 4580
[4] Eachus R S and Graves R E 1974 *J. Chem. Phys.* **61** 2860
[5] Wilkens J, DeGraag D P and Helle J N 1965 *Phys. Lett.* **19** 178
[6] Shock J R and Rogers M T 1975 *J. Chem. Phys.* **62** 2640
[7] Olm M T, Niklas J R, Spaeth J-M and Symons M C R 1988 *Phys. Rev.* B **38** 4343
[8] Vercammen H, Ceulemans T, Schoemaker D, Moens P and Vandenbroucke D 1996 *Proc. IS&T 49th Ann. Conf. (1996)* p 54
[9] Schweizer S and Spaeth J-M 1997 *J. Phys. Chem. Solids* **58** 859
[10] Bus'ko E A, Burkov K A and Kalinin S K 1970 *J. Anal. Chem.* **25** 827
[11] Endo K and Saikawa M 1990 *J. Photogr. Sci.* **38** 210
[12] Moens P, Vercammen H, Vandenbroucke D, Callens F and Schoemaker D 1996 *Proc. IS&T 49th Ann. Conf. (1996)* p 56
[13] Zdrakova M, Vrielinck H, Callens F, Boesmann E, Vercammen H and Schoemaker D 1997 *J. Appl. Phys.* **82** 2476
[14] Rist G H and Hyde J S 1970 *J. Chem. Phys.* **52** 4633
[15] Hoffman B M, Venters R A and Martinsen J 1985 *J. Magn. Reson.* **62** 537
[16] Hurst G C, Henderson T A and Kreilick R W 1985 *J. Am. Chem. Soc.* **107** 7294
[17] Spaeth J-M, Niklas J R and Bartram R H 1992 *Structural Analysis of Point Defects in Solids* (Springer)
[18] Baetzold R C 1997 *J. Phys. Chem.* B **101** 1130
[19] Hyde J S, Rist G H and Erikson L E 1968 *J. Phys. C: Solid State Phys.* **72** 4269